AGU PUBLICATIONS

JGR

Journal of Geophysical Research: Space Physics

RESEARCH ARTICLE
10.1002/2017JA024594

Key Points:
- Proton and sodium ions in Mercury's southern plasma mantle have mean number densities of ~1.5 and 0.004 cm^{-3}, respectively
- The highest estimates of mantle proton and sodium flux supply to the plasma sheet are 1.5×10^8 cm^{-2} s^{-1} and 0.8×10^8 cm^{-2} s^{-1}, respectively
- An average cross-electric magnetospheric potential of ~19 kV is determined, which is enhanced for increased IMF strength and $-B_Z$

Supporting Information:
- Supporting Information S1

Correspondence to:
J. M. Jasinski,
jjasinski@umich.edu

Citation:
Jasinski, J. M., Slavin, J. A., Raines, J. M., & DiBraccio, G. A. (2017). Mercury's solar wind interaction as characterized by magnetospheric plasma mantle observations with MESSENGER. *Journal of Geophysical Research: Space Physics*, *122*, 12,153–12,169. https://doi.org/10.1002/2017JA024594

Received 13 JUL 2017
Accepted 18 SEP 2017
Accepted article online 21 SEP 2017
Published online 15 DEC 2017

Mercury's Solar Wind Interaction as Characterized by Magnetospheric Plasma Mantle Observations With MESSENGER

Jamie M. Jasinski[1], James A. Slavin[1], Jim M. Raines[1], and Gina A. DiBraccio[2]

[1]Climate and Space Sciences and Engineering, University of Michigan, Ann Arbor, MI, USA, [2]Solar System Exploration Division, NASA Goddard Space Flight Center, Greenbelt, MD, USA

Abstract We analyze 94 traversals of Mercury's southern magnetospheric plasma mantle using data from the MESSENGER spacecraft. The mean and median proton number densities in the mantle are 1.5 and 1.3 cm^{-3}, respectively. For sodium number density these values are 0.004 and 0.002 cm^{-3}. Moderately higher densities are observed on the magnetospheric dusk side. The mantle supplies up to 1.5×10^8 cm^{-2} s^{-1} and 0.8×10^8 cm^{-2} s^{-1} of proton and sodium flux to the plasma sheet, respectively. We estimate the cross-electric magnetospheric potential from each observation and find a mean of ~19 kV (standard deviation of 16 kV) and a median of ~13 kV. This is an important result as it is lower than previous estimations and shows that Mercury's magnetosphere is at times not as highly driven by the solar wind as previously thought. Our values are comparable to the estimations for the ice giant planets, Uranus and Neptune, but lower than Earth. The estimated potentials do have a very large range of values (1–74 kV), showing that Mercury's magnetosphere is highly dynamic. A correlation of the potential is found to the interplanetary magnetic field (IMF) magnitude, supporting evidence that dayside magnetic reconnection can occur at all shear angles at Mercury. But we also see that Mercury has an Earth-like magnetospheric response, favoring $-B_Z$ IMF orientation. We find evidence that $-B_X$ orientations in the IMF favor the southern cusp and southern mantle. This is in agreement with telescopic observations of exospheric emission, but in disagreement with modeling.

1. Introduction

The magnetospheric plasma mantle is located in the nightside high-latitude magnetotail. The observed plasma originates from the solar wind, entering the magnetosphere at the dayside magnetopause via magnetic reconnection. Magnetic reconnection between the interplanetary magnetic field (IMF) and the dayside magnetospheric field occurs when the fields are antiparallel. This drives the dynamics at the terrestrial magnetospheres by opening closed magnetospheric field lines on the dayside, transporting them through the lobes and closing them on the nightside in the magnetospheric current sheet. The closed magnetic flux is then transported to the dayside magnetosphere where it can once again be opened by dayside magnetopause reconnection. This is called the Dungey cycle (Dungey, 1961). The top half of Figure 1 shows a schematic of Mercury's magnetosphere. The Sun is to the left, and the dashed lines show the bow shock ("BS") and magnetopause ("MP").

After dayside magnetic reconnection occurs, shocked solar wind plasma is able to enter a magnetosphere through the dayside high-latitude cusps, which is shaded gold in Figure 1 (e.g., Jasinski et al., 2014; Lockwood & Smith, 1994; Raines et al., 2014; Reiff, Hill, & Burch, 1977). However, as the field line convects antisunward after reconnection, some of the particles that originally entered the cusp will eventually mirror and travel along the magnetic field line away from the planet. This region of the magnetosphere is the plasma mantle. At Mercury, the plasma mantle is located in the high-latitude nightside magnetosphere (DiBraccio, Slavin, Raines, et al., 2015) where plasma originating from the magnetosheath flows in a direction away from the cusps (and away from the planet), down the magnetotail along field lines inside of the magnetopause (shaded red in Figure 1). The mantle is an important feature to study as the observed particles are present due to reconnection and this region can characterize a magnetosphere's interaction with the solar wind as well as being a measure of the sources and sinks of magnetospheric plasma.

The first detection of the Earth's plasma mantle was reported from the Vela satellite observations as a thick boundary layer surrounding the magnetotail where antisunward magnetosheath protons were observed

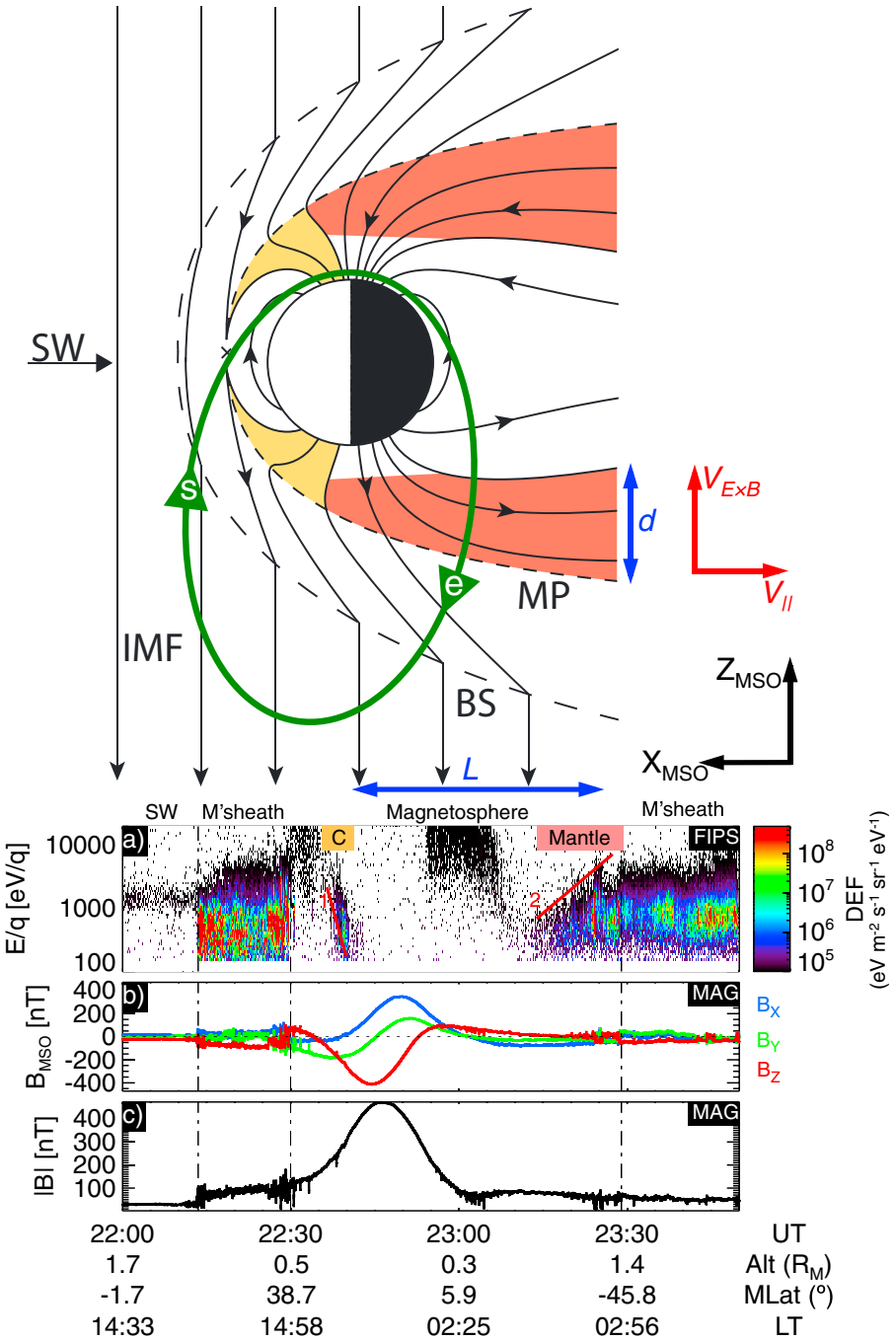

Figure 1. An example of a MESSENGER trajectory on an average orbit in Mercury's magnetosphere and the associated observations. (top) A schematic of Mercury's magnetic field with the cusp (yellow shading) and mantle (red shading) highlighted and the corresponding trajectory of MESSENGER (shown in green). The directions of the drift velocity ($\mathbf{V}_{E\times B}$), parallel velocity ($\mathbf{V}_{||}$), and the thickness d and length L are also shown. (bottom) (a) FIPS proton counts with the observed energy dispersions in the cusp (1) and mantle (2) underlined in red, (b) the three components of the observed magnetic field (MAG) in MSO coordinates, and (c) magnitude of the magnetic field (MAG). The following acronyms are used: "SW" for solar wind, "M'sheath" for the magnetosheath, "IMF" for the interplanetary magnetic field, "BS" for the bow shock, "MP" for the magnetopause, and "DEF" for differential energy flux.

within the nightside magnetopause (Hones et al., 1972; Sckopke et al., 1973). The thickness of this mantle was found to be 0.5–4 R_E (where R_E is the radius of the Earth), with the flow speeds positively correlated to that of the magnetosheath, and the proton number density decreasing (from ~10 to 0.01 cm^{-3}) with increasing distance from the magnetopause (Rosenbauer et al., 1975). The global thickness of the plasma mantle was

observed to vary with interplanetary magnetic field (IMF) orientation, with a thicker mantle present for strongly southward IMF orientations when dayside magnetopause reconnection is enhanced (Sckopke et al., 1976). Pilipp and Morfill (1978) also showed that the mantle is a source of material for the plasma sheet as the solar wind particles are able to $\mathbf{E} \times \mathbf{B}$ drift from the high-latitude tail toward the central plasma sheet. Ionospheric ion outflow is another source of material for the plasma sheet (e.g., Horowitz & Moore, 1997).

Magnetohydrodynamic models also describe the plasma mantle as a standing slow-mode expansion fan, whereby the plasma mantle becomes thicker with increasing distance downtail (Sanchez & Siscoe, 1990; Siscoe & Sanchez, 1987). An important resulting effect from this increase in thickness, and the key observational characteristic of the plasma mantle, is a particle velocity dispersion. The particles are flowing antisunward with a downtail field-aligned velocity ($\mathbf{V}_{||}$). There is also a motion of the particles perpendicular to the magnetic field due to the $\mathbf{E} \times \mathbf{B}$ drift ($\mathbf{V}_{perp} = \mathbf{V}_{E \times B}$). The combination of these two velocities results in a motion downtail as well as toward the plasma sheet (Figure 1). This means particles with a lower $\mathbf{V}_{||}$ will arrive at the plasma sheet closer to the planet, while particles with larger $\mathbf{V}_{||}$ travel further downtail before arriving in the plasma sheet. Therefore, an energy dispersion is observed in the plasma mantle (e.g., Sckopke & Paschmann, 1978; Slavin et al., 1985) for a spacecraft traveling orthogonal to the magnetopause, where a dropout of higher energy particles is observed closer to the plasma sheet. The dispersion is highlighted by a red line labeled "2" in Figure 1a.

In order to characterize the mantle at Mercury and understand solar wind-planetary interaction, we used data from the MErcury Surface, Space ENvironment, GEochemistry, and Ranging (MESSENGER) spacecraft, which was in orbit around Mercury in 2011–2015. Results from the MESSENGER mission have shown that the magnetosphere of the smallest planet is very dynamic with a short Dungey-cycle magnetospheric-convection time scale of ~3 min (Slavin et al., 2009, 2010), in comparison to a 1–3 h at Earth (e.g., Huang, 2002; Siscoe, Ness, & Yeates, 1975; Tanskanen, 2009). At the dayside, magnetic reconnection is observed to occur between the planetary field and the IMF even at small magnetic shear angles of ~30° (DiBraccio et al., 2013), in contrast to Earth where shear angles of ~90–270° are required (Burton, McPherron, & Russell, 1975; Mozer & Retin'o, 2007). Flux transfer event (FTE) observations occur when reconnection occurs at multiple x-lines along the dayside magnetopause that twist the magnetic fields into a rope-like configuration (e.g., Fu & Lee, 1985; Jasinski et al., 2016; Russell & Elphic, 1978, 1979). FTEs at Mercury are extremely common and have been observed as "FTE showers" with separations of ~8 s between events (Slavin et al., 2012). At Earth, FTEs are observed to occur every ~8 min (Rijnbeek et al., 1984). Imber et al. (2014) conservatively estimated that FTEs can supply up to a third of the open magnetic flux content at the magnetosphere at Mercury, in comparison to the 2% estimated at Earth (Milan, Provan, & Hubert, 2007). Therefore, FTEs are more likely to play an important role in supplying the mantle with plasma at Mercury, as well as the plasma mantle being an important source of plasma in the Mercury's magnetosphere. The first observation of the southern plasma mantle at Mercury was reported by DiBraccio, Slavin, Raines, et al. (2015). In this study, the authors presented two traversals of the mantle on the same day, where an ion energy-latitude dispersion was observed as well as frequent FTE observations in the adjacent magnetosheath. From these dispersions the cross-magnetospheric electric potentials were estimated to be ~23 and ~29 kV.

In this paper, we present a survey of southern plasma mantle observations completed by the MESSENGER spacecraft between 2011 and 2015 in order to better understand the plasma mantle contribution to magnetospheric dynamics at Mercury and quantify its characteristics. We first describe the instrumentation, followed by the selection criteria from observations for our study and the results.

2. Instrumentation

Data from the following MESSENGER instrumentation were used for this analysis: the fast imaging plasma spectrometer (FIPS) (Andrews et al., 2007) and the magnetometer (MAG) (Anderson et al., 2007).

FIPS was a time-of-flight mass spectrometer that measured ions with an energy-per-charge range of 46 eV–13 keV/q, a mass-per-charge range of 1–60 amu/q, with a time resolution of ~8 s. The angular resolution was ~15°, and the effective field of view of the instrument was ~1.15 π sr as ~0.25 π sr was blocked by the spacecraft sunshade. MAG was a fluxgate magnetometer mounted on a 3.6 m long boom, with a

resolution of 0.047 nT and a maximum time resolution of 20 vectors s^{-1}. The magnetic field measurements are presented in Mercury solar orbital (MSO) coordinates, where X is in the planet-Sun direction, $-Y$ points toward planetary orbital velocity vector direction, and Z completes the right-hand set and points northward.

3. Observations

3.1. Overview for a Typical MESSENGER Orbit

For trajectories close to the noon-midnight meridian, the MESSENGER spacecraft crossed the nightside southern magnetopause. This means plasma mantle detections can occur between the tail lobe (low plasma density and high magnetic field strength) and the magnetosheath (high plasma density and lower magnetic field strength), both adjacent to the mantle. Depending on the direction of the trajectory (planetward or anti-planetward), the observations of the region of interest are in the chronological order of magnetosheath $>$ mantle $>$ lobe for a planetward trajectory and the opposite for an outward trajectory.

An example of this typical trajectory and the corresponding MESSENGER observations are displayed in Figure 1. The data for the trajectory (data panel a) start and end at the arrowheads (left and right, respectively, clockwise). The observations begin in the solar wind, where low ion fluxes are measured near ~1 keV. The spacecraft then crossed the bow shock (BS) and entered the magnetosheath (M′sheath) at ~22:13 UT, where the magnitude of the magnetic field increased from ~25 to ~80 nT, and FIPS observed the dense, shocked solar wind plasma (a). At ~22:30 UT the spacecraft crossed the magnetopause (MP) and entered the magnetosphere where tenuous energetic plasma was observed, followed by the cusp (gold) where magnetosheath plasma with an energy-latitude dispersion (higher energies observed at lower latitudes—underlined in red and labeled "1") was observed at ~23:37 UT. The spacecraft then observed the northern tail lobe before crossing the plasma sheet (~23:00 UT) where energetic plasma was observed and the B_X component (blue in panel b) of the magnetic field was equal to ~0 nT. Before entering the plasma mantle, the southern lobe was observed (as indicated by the $-B_X$ orientation) where no plasma is detected within the threshold of FIPS. While in the mantle, higher energies were observed closer to the magnetopause due to the effect of $\mathbf{V}_{E \times B}$ as described above (this dispersion is underlined in red and labeled "2"). The spacecraft crossed the magnetopause once again where it observed the magnetosheath.

Large fluctuations in the magnetic field data can be seen at the magnetopause (the magnetopause is marked by the middle and right vertical dashed lines), as well as in the plasma sheet. These are largely due to the presence of flux ropes, with flux transfer events being observed at the magnetopause and plasmoids in the plasma sheet (e.g., DiBraccio, Slavin, Imber, et al., 2015; Imber et al., 2014; Slavin et al., 2012), as well as dipolarization fronts in the plasma sheet (Sun et al., 2016; Sundberg et al., 2012).

The 0.196 R_M northward offset of Mercury's dipole (Anderson et al., 2011) results in different features for the plasma in the northern and southern parts of the magnetosphere, resulting in a plasma asymmetry in the nightside (Korth et al., 2014). The asymmetry affects the plasma in the cusps and therefore the resulting plasma observed in the northern or southern mantle. Due to the trajectory of MESSENGER we only survey observations from the southern mantle. We do not expect the northern mantle to be similar to the observed southern mantle due to the above-mentioned asymmetry.

3.2. Data Selection Method

The plasma mantle observations were identified by the ion energy dispersion observed in the FIPS data similarly to the first plasma mantle observations at Mercury (DiBraccio, Slavin, Raines, et al., 2015). MESSENGER observations of two example mantle traversals can be seen in Figures 2 and 3, for an inbound and outbound trajectory, respectively. Figure 2 shows a scenario where the spacecraft passed from the southern lobe into the plasma mantle (bounded by the two vertical lines) and out into the magnetosheath, while in Figure 3, MESSENGER crossed the boundaries in the reverse order. Figures 2 and 3 are in the same format, with proton flux, proton number density, and sodium counts all from FIPS shown in Figures 2a–2c and 3a–3c, respectively. Proton number density was estimated using a forward modeling technique, a method used in previous papers (Gershman et al., 2013; Raines et al., 2011), the values of which have been delivered to the Planetary Data System (Ho et al., 2016). This is followed by magnetometer measurements, including the three

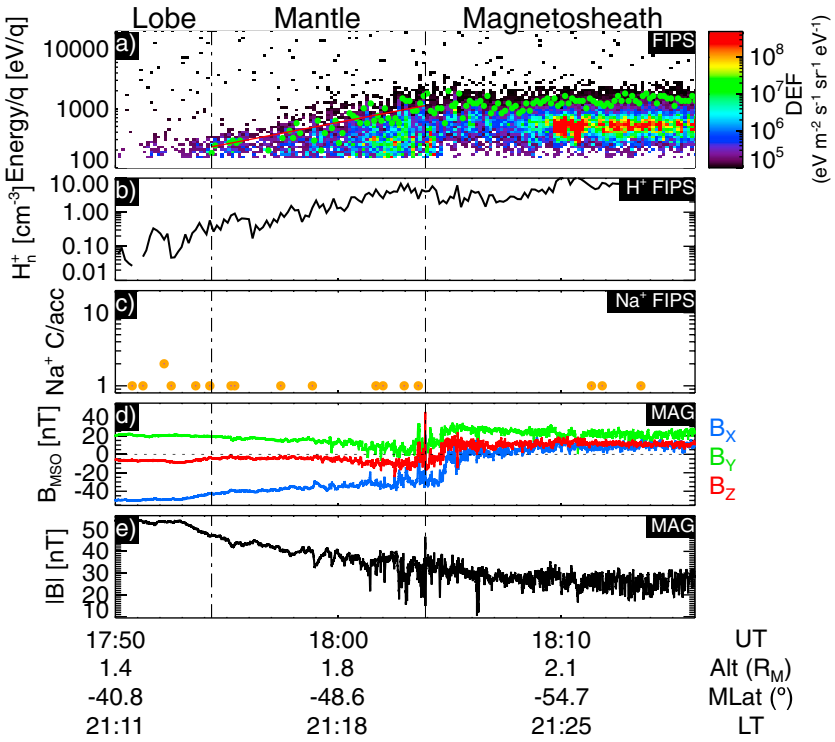

Figure 2. An example of a mantle observation on an outbound (antiplanetward) trajectory from 10 October 2011. The southern lobe and magnetosheath are observed before and after the plasma mantle, respectively. (a) FIPS ion energy spectrogram showing the differential energy flux (DEF). The green dots represent the lowest energy bin observed to have a signal-to-noise ratio of ≥2.0, and a fit to these energies is shown in red to highlight the energy dispersion observed in the FIPS data. (b) FIPS calculated proton density moment, (c) FIPS sodium counts per accumulation, (d) three components of the magnetic field observed by MAG, and (e) magnetic field magnitude (MAG).

components of the magnetic field in MSO coordinates and magnitude shown in panels Figures 2d and 2e and 3d and 3e, respectively.

The inner boundary of the mantle (adjacent to the southern lobe, where no plasma is observed by FIPS) was determined by the inner most signal-to-noise ratio (SNR) ≥ 2 in the FIPS measured proton counts. This can be seen in Figures 2a and 3a, where the highest energy bin with an SNR ≥ 2 for each FIPS accumulation is marked by a green dot. The inner boundary of the mantle, adjacent to the tail lobe, is marked by the first (second) vertical dashed line in Figure 2a (Figure 3a) where the SNR meets this selection threshold. The SNR threshold also makes the ion energy dispersion more clear (highlighted by the red line).

The outer boundary of the mantle, adjacent to the magnetosheath, was selected on the basis of the magnetic field variation (ΔB) observed by MAG. This is due to the magnetic field varying significantly more in the magnetosheath adjacent to the mantle than within the magnetosphere. The magnetic field variation was calculated using

$$\Delta B_i = \sqrt{\frac{(b_i - B_{\mathrm{ave}_i})^2}{20}} \tag{1}$$

where $B_{\mathrm{ave\_}i}$ is a 21-point running average (i.e., ~1 s average) centered at data point b_i. A smoothing average filter was applied to ΔB_i by calculating a thousand-point average. The outer boundary of the mantle was selected when the magnetic field variability ΔB_i was drastically greater than its thousand point average (defined as when $\Delta B_i > 3.7\ \Delta B_{1000\text{-point-average}}$). Initially, the outer boundary selection process was focused on finding where the magnetic field rotated as the spacecraft crossed the magnetopause boundary (as can be seen at ~18:10 UT in Figures 2d and 2e). However, not all the magnetopause crossings present a field rotation, and therefore, we chose to use the magnetic field variability instead as it is more reliable.

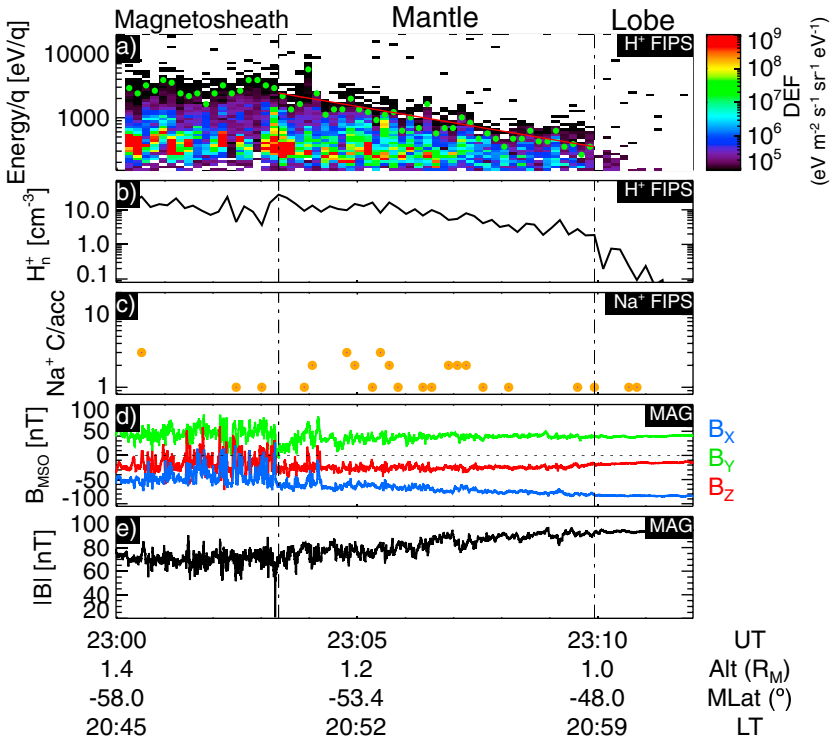

Figure 3. An example of a mantle observation on an inbound trajectory (planetward and equatorward) from 10 April 2015. The order in which the regions are observed is opposite to Figure 2, with the magnetosheath observed before and the lobe after the mantle. The format is the same as Figure 2.

A total of 94 mantle crossings were identified, including the two observations reported by DiBraccio, Slavin, Raines, et al. (2015). As can be seen in Figure 4, plasma mantle observations occurred in the southern nightside region of the magnetosphere. The observations are in the southern hemisphere only because of the orbital configuration of MESSENGER that never had the opportunity to explore the northern mantle region. The location of the observations can be seen in Figure 4, shown in aberrated Mercury solar orbital (MSO) coordinates. The coordinates are aberrated to account for the high orbital velocity of the planet (39–59 km/s), which results in the effective solar wind arrival vector being offset by ~7 deg from the X_{MSO} direction. The orbital velocity varies over the Mercury's year due to its highly eccentric orbit. The degree of aberration is also dependent on the solar wind velocity. Here we use the aberration determined by Boardsen et al. (2010), which calculated the aberration angle for each day by assuming a 410 km/s solar wind speed.

Figure 4 also shows the spatial distribution of the average proton (Figures 4a–4c) and sodium (Figures 4d and 4e) number densities in the plasma mantle in the three different planes. The density in this figure is the average measured number density of every measurement FIPS made in Mercury's plasma mantle during a given traversal. To ensure that the results were not affected by the FIPS field of view (FOV), we checked for density variations in the different instrument look directions. During the mantle observations, the FIPS FOV was ~42–270° from the *Y* MSO direction in the *Y-Z* MSO plane (0° and 90° being in the *Y* and *Z* MSO directions, respectively). The density trends discussed below were the same for FOV bins of 45–135° and 135–225°, which means that they are not a result of instrument effects but are physical results. It can be generally seen that the mantle is denser closer to the magnetopause. This can be seen more clearly for a specific mantle crossing, in a density line plot shown in Figure 2b. As MESSENGER approaches the magnetopause, the plasma density increases gradually. Figures 4b and 4c also show a modest increase in density of the plasma mantle toward dusk. This is due to the centrifugal drift that the ions experience close to the planet due to the curvature of the magnetic field (e.g., Delcourt et al., 2003). The resulting drift is in the duskward direction, which explains the higher densities in the plasma mantle in the dusk sector. Figures 4d–4f are in the same format as Figures 4a–4c but are shown for sodium number density. The sodium observation follows a similar trend as the protons, with slightly higher densities in the dusk sector. However, it does not appear that the sodium is denser nearer the magnetopause.

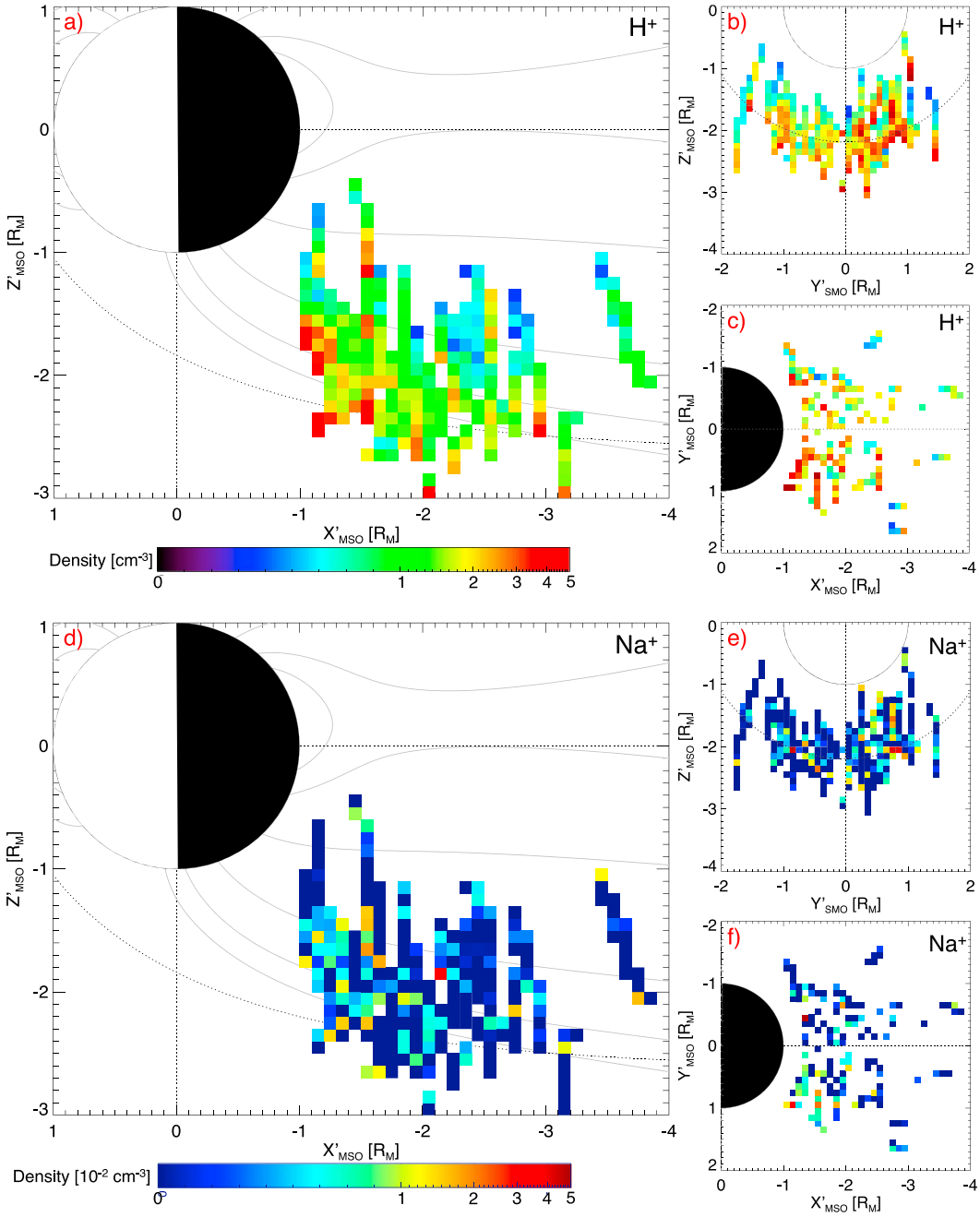

Figure 4. The average (a–c) proton and (d–f) sodium density maps of the observed plasma mantle events by the MESSENGER FIPS instrument. The locations are shown in abberrated Mercury solar orbital (MSO) coordinates where X′ points from Mercury's center toward the oncoming solar wind, Z′ is perpendicular to the orbital plane pointing northward, and Y′ completes the right-hand set. (a and d) A view from dusk (X′–Z′) with model magnetospheric field lines shown in gray obtained from the global magnetospheric MHD model of Mercury (Jia et al., 2015). (b, c and e, f) Projections of the (right) X′–Y′ and (left) Y′–Z′ planes. A model magnetopause is calculated using the Shue et al. (1997) magnetopause formulation, with a superimposed dipole offset of 0.196 R_M, which has been found at Mercury (Anderson et al., 2011, 2012; Johnson et al., 2012).

3.3. IMF Correlation

The plasma mantle observations were also compared to the IMF conditions. IMF observations to the nearest bow shock crossing were averaged over a 2 min interval. We also calculated the average over a 20 min interval to provide an estimate of the variability of the IMF. Figures 5a and 5b show histograms of the average plasma mantle proton and sodium number density, respectively, organized by IMF orientation in the north-south direction, B_Z. From these figures we can see that the observation of the plasma mantle is

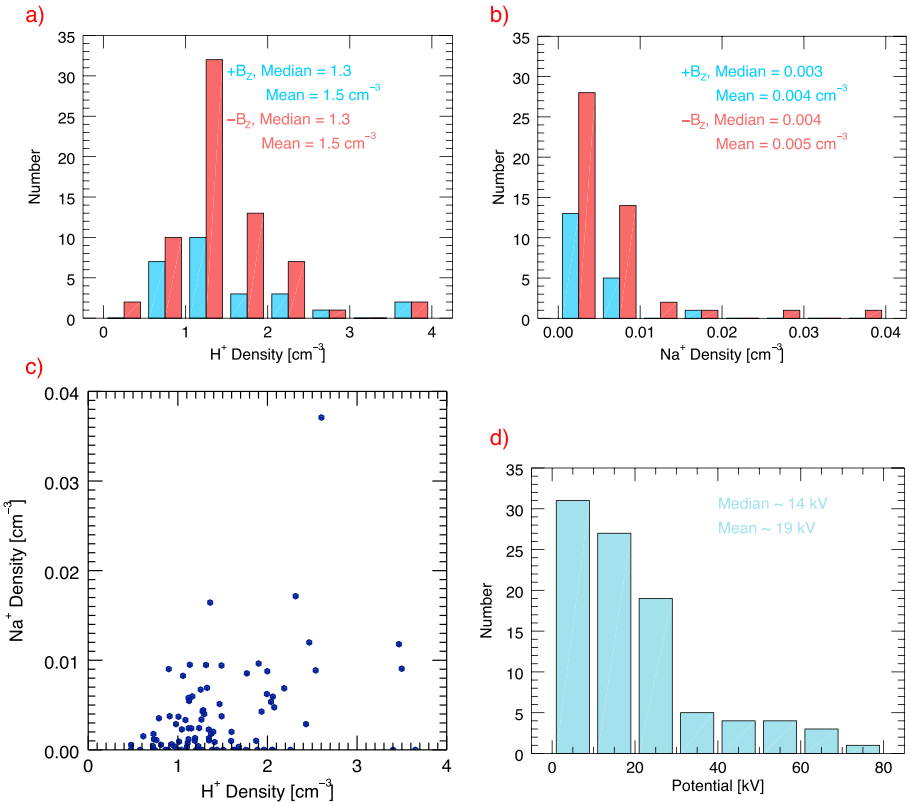

Figure 5. Histograms of the averaged (over event) (a) proton and (b) sodium number density measurements. The densities are also divided into the estimated solar wind B_Z orientation ($-B_Z$ is red, $+B_Z$ is blue). (c) The sodium-to-proton density relationship. (d) A histogram of the cross-electric magnetospheric potential estimates.

more likely to occur for $-B_Z$ conditions. The plasma mantle is also more likely to be denser during $-B_Z$. Like at Earth, these observations are due to $-B_Z$ resulting in higher reconnection rates at the dayside subsolar magnetopause, which are more likely to inject larger numbers of plasma into the magnetosphere, which are eventually observed in the plasma mantle.

Figure 5c shows the observed sodium ion densities in comparison to proton density measurements (both observed in the mantle). Sodium observations are common at Mercury's magnetosphere and are present due to sputtering at the planet's surface (e.g., Raines et al., 2014). For times when FIPS observes sodium, the sodium density has a strong dependence on the proton density (i.e., we see higher sodium with higher proton densities). However, we do not always observe sodium in the plasma mantle. We also did not observe a dependence of the sodium density on the IMF magnitude.

3.4. Estimating the Electric Potential and Plasma Flux

3.4.1. Calculation of the Magnetospheric Cross-Electric Potential

From the plasma mantle observations (FIPS and MAG) we are able to estimate the electric field **E**, using $\mathbf{E} = -\mathbf{V}_{E\times B} \times \mathbf{B}$, where $\mathbf{V}_{E\times B}$ is the drift velocity and **B** is the magnetic field. We then use these values of **E** to estimate the magnetospheric cross-electric potential (Φ), as described by DiBraccio, Slavin, Raines, et al. (2015). Considering the high-latitude trajectory of MESSENGER, we assume that the spacecraft was traveling orthogonal to the magnetopause. Therefore, we estimate $\mathbf{V}_{E\times B}$ by assuming $\mathbf{V}_{E\times B} \sim V\theta$, where θ is the dispersion wedge angle calculated geometrically from L and d, which are shown in Figure 1. L is the distance from the day-night terminator in the X_{MSO} direction, and d is the thickness of the mantle in the Z_{MSO} direction. These are calculated using the position of the spacecraft in the magnetosphere and its distance from the magnetopause. V is the plasma velocity observed by the FIPS instrument. This is calculated from a weighted mean of proton energy distributions based on the flux measurements. We then calculate E using $\mathbf{V}_{E\times B}$ and the average observed magnetic field B by MAG. The cross-electric potential is determined by $\Phi = Ed_{tail}$, where d_{tail} is the magnetotail width and is taken to be ~5 R_M consistent with the average values

estimated previously (Sun et al., 2015; Winslow et al., 2013). For each mantle crossing, this method is completed for every FIPS measurement over a single traversal and then averaged to produce a potential estimation for every event. For more details about this method, please refer to DiBraccio, Slavin, Raines, et al. (2015).

There are uncertainties associated with our calculations. First, the calculation is dependent on our selection criteria, specifically the location of the outer boundary of the plasma mantle (the magnetopause) from the observed magnetic variation, ΔB_i. DiBraccio, Slavin, Raines, et al. (2015) visually identified the magnetopause based on magnetic field rotations. For this study, however, there is not always a clear rotation at the boundary and our approach of utilizing magnetic field variations is more appropriate for a larger data set. It should be noted that this method is more likely to select the most inner boundary of the magnetopause; therefore, our electric potential calculations are likely lower limits. In comparison to the DiBraccio, Slavin, Raines, et al. (2015) calculations for the two mantle events observed on 10 November 2012 (~23 and ~29 kV), we calculated potentials of ~21 and ~23 kV, respectively. This corresponds to a difference of ~9 and ~20% to DiBraccio, Slavin, Raines, et al. (2015) calculations. Using their selection criteria for the example shown in Figure 2, the magnetopause would be selected at the field rotation observed at 18:03:45 UT (one time tick to the right of the second vertical dashed line in Figure 2). The difference in the calculated potential from their method in comparison to ours is the same to zero decimals. Similarly, we calculated the potentials for the event that shows the largest time difference between the field rotation and our selection time. For the 28 September 2011 mantle event, the calculated potentials using the DiBraccio, Slavin, Raines, et al. (2015) method (of magnetopause identification) and ours are ~23 kV and ~17 kV, respectively. This represents a difference of ~26%. Therefore, we estimate that our calculations may underestimate the potential by an upper limit of ~25% for some (but not all) events. To account for this underestimation we present our estimated potentials as 125% of the values calculated from this method.

Other uncertainties manifest themselves from the method we have used here. The width of the magnetotail (d_{tail}) is the average value estimated by Winslow et al. (2013), which may vary by up to 2 R_M. The value of L may also vary depending on where the solar wind particles were injected in the cusp (Raines et al., 2014) and where they mirror along their trajectory. Therefore, our L estimate is most likely a lower value, but it would not increase by more than ~0.5 R_M, since the dayside subsolar magnetopause is located on average less than 0.5 R_M from the surface of Mercury (Winslow et al., 2013). The FIPS instrument does not sample the complete plasma velocity distribution due to its field of view constrictions, and therefore, the speed may be higher than the ones calculated here (Gershman et al., 2012).

A histogram of the estimated cross-magnetospheric electric potential for each plasma mantle event (corrected for the underestimation as discussed above) is shown in Figure 5d. We estimate a wide range of potentials at Mercury (1–74 kV). The average is ~19 kV and the median ~ 13 kV. These values are lower than previous estimates (e.g., DiBraccio, Slavin, Raines, et al., 2015; Imber et al., 2014). However, our study includes all MESSENGER observations and does not focus on large amplitude events (such as the large FTEs observed by Imber et al., 2014 and the large mantle dispersion observed by DiBraccio, Slavin, Raines, et al., 2015). Therefore, our study includes quiet magnetospheric conditions as well as the extreme events. We do observe a large variety of potentials that shows that Mercury's magnetosphere is very dynamic and active.

3.4.2. Estimating the Plasma Flux Supply to the Plasma Sheet

Using the estimated $\mathbf{E} \times \mathbf{B}$ drift velocity from the previous section, we have also estimated the subsequent particle flux that the plasma mantle supplies to the nightside plasma sheet located in the magnetotail. We assumed the protons had pitch angles of 45° (from FIPS measurements the observed pitch angles are largely 45–90°), with the magnetic field directed antisunward. We estimated the particle energies that would be lost downtail (past the nightside tail reconnection location) based on their observed energies (and therefore velocities) in comparison to the estimated $\mathbf{V}_{E \times B}$. Here we assume that the nightside tail reconnection location is at ~3 R_M (Poh et al., 2017). We estimated the integrated flux in the mantle using this energy cutoff to estimate the proton flux supply to the plasma sheet. This was done for every FIPS accumulation and then averaged for each mantle event (similarly to the cross-magnetospheric electric potential discussed above).

Due to the locations of our plasma mantle observations occurring at large downtail distances (up to -4 R_M in the X'-MSO direction), most of the observed protons during our crossings are lost downtail. Only 7 of the 94 mantle crossings present plasma that enters the plasma sheet planetward of the reconnection location. If we

assume field-aligned pitch angles of 0°, this number falls to 5. Assuming the particles have a close-to-perpendicular pitch angles (80°), 38 of the mantle events measured protons that would populate the plasma sheet. The largest estimated proton flux to the plasma sheet from a single mantle event is 1.5×10^8 cm^{-2} s^{-1}. For the calculations assuming that the proton pitch angle is 80°, the average plasma flux to the plasma sheet from our events (for when the mantle is able to supply the plasma sheet) was 3.6×10^7 cm^{-2} s^{-1}. Using the same method, we estimated the flux for sodium entering the plasma sheet and found the largest to be 0.8×10^8 cm^{-2} s^{-1} and an average of 0.6×10^8 cm^{-2} s^{-1}. The average value is half that for the protons. Even though the observed fluxes of protons are much greater in the mantle than the sodium, due to the higher mass of sodium, the parallel velocity is lower; therefore, less sodium is lost downtail in comparison to protons and a larger fraction of the sodium enters the plasma sheet.

3.5. When Do We Not Observe the Mantle?

We have also investigated periods in MESSENGER's orbit when the spacecraft did not observe the plasma mantle. We investigated magnetopause crossings in the nightside of the magnetosphere within ±1 R_M in abberated Y'_{MSO} direction. These trajectories can be seen in Figures 6a and 6b (this is MESSENGER's trajectory for 5 min equatorward of the magnetopause crossing). For consistency with plasma mantle observations, we also removed any trajectories that did not have the same FOV for FIPS as the mantle crossings. The mantle was observed with FOV angles greater than 45° away from the $+Y_{MSO}$ direction. This removes ~5% of the remaining trajectories. With these criteria there were 957 times when the mantle was not observed. We obtained the IMF conditions for these events using the same method that we used for the plasma mantle events (discussed above).

Figures 6c–6f compare the IMF conditions when the plasma mantle was observed (red) and not observed (blue). Figure 6c shows the comparison of the IMF magnitude. For both, the distribution peaks at the 25 nT centered bin. However, we can see that the mantle is much more likely to be seen for IMF magnitudes at and below this value. We will show that the magnetospheric potential increases for larger IMF magnitudes (shown below in section 3.6). However, this figure shows that we are less likely to observe the mantle for the much higher magnitudes. This is because higher field strengths at the dayside magnetopause reconnection location will produce higher parallel electric fields (Li et al., 2017) that are more likely to create particle distributions with more field-aligned pitch angle velocities (Egedal, Daughton, & Le, 2012). This results in less particles mirroring, and instead, more particles are lost to the surface. This means that a plasma mantle is less likely to be formed for very high IMF magnitudes.

Figure 6d compares the B_Z orientation of the IMF to when we see and do not see the plasma mantle. From this histogram, we conclude that the mantle is much more likely to be observed for a southward ($-B_Z$) pointing IMF than a northward one.

3.5.1. Dependence on the IMF B_X Component

Figures 6e and 6f show the mantle observation with the B_X IMF component for southward ($-B_Z$) and northward ($+B_Z$) directed IMF, respectively. We separated the B_X observations into northward and southward B_Z to try and eliminate the possibility of mistaking any radial dependency on the north-south component of the IMF. We can see that for both cases we are more likely to observe (in the southern magnetosphere for our trajectory) plasma mantle for $-B_X$ than for $+B_X$. From the distribution and the comparison of the means and medians between when MESSENGER observes the mantle and when it does not, it appears that the B_X component is more likely to have a stronger effect when B_Z is northward, and therefore, reconnection is occurring at the high-latitude magnetopause.

Our B_X correlation results are inconsistent with models (Massetti et al., 2007; Sarantos et al., 2001), where the results indicate the opposite correlation of $+B_X$ conditions in IMF favoring the southern cusp (we observe $-B_X$ conditions favoring the southern mantle and therefore the southern cusp). However, observations of exospheric sodium emission and their correlation to the IMF (specifically B_X) agree with our results (Mangano et al., 2015; Massetti et al., 2017). Mangano et al. (2015) had the strongest correlation (78%) to their observation of enhanced emission in the northern exosphere with $+B_X$ and also more frequent (73%) when the IMF had large magnitudes (>25 nT). Massetti et al. (2017) also mentioned that they observe a B_X correlation that is opposite to the previous modeling work; however, they do not discuss this further. The modeling does not explicitly explore varying B_X with consistent B_Y and B_Z values and largely just explores the behavior

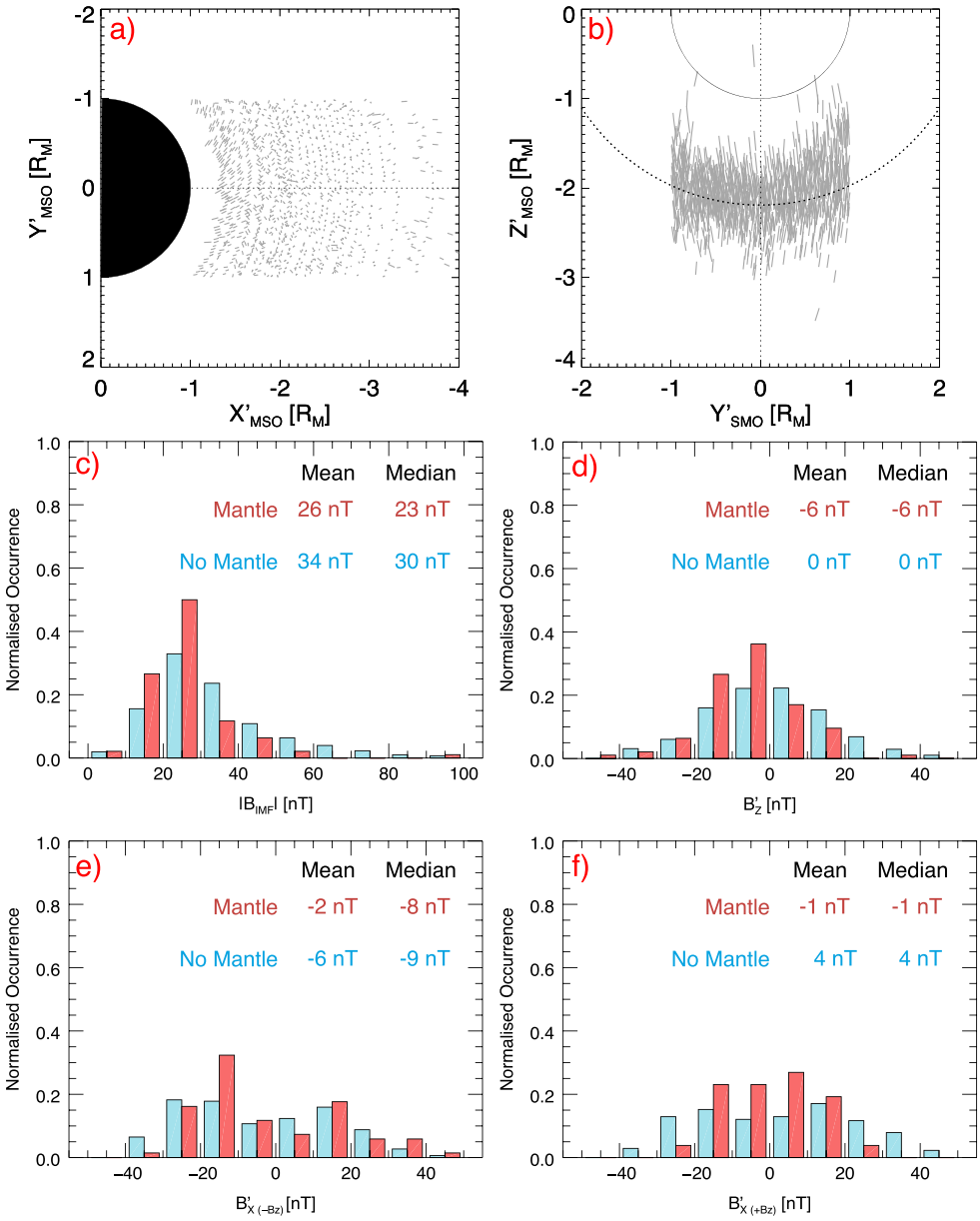

Figure 6. Results regarding the analysis of when we do not observe the plasma mantle. (a and b) The trajectory of MESSENGER for 5 min inward the magnetopause in the X′–Y′ and Y′–Z′ planes, respectively (in abberated MSO coordinates). (c and d) Histograms of the IMF magnitude and B_Z conditions for when we see the mantle (red) and do not see the mantle (blue). (e and f) The B_X component strength for $-B_Z$ and $+B_Z$, respectively.

with regards to typical parker spiral conditions. We therefore suggest that previous modeling studies do not agree with the growing body of observational results, which may be due to this lack of consistency.

3.6. Other Solar Wind Correlations

Comparisons of the solar wind to the estimated cross-electric magnetospheric potential are shown in Figure 7. The error bars are the representations of the variability of the IMF observed over the 20 min interval in comparison to the 2 min average (discussed above). Shown in gray are box and whisker plots to represent the interquartile range and the median (see caption for details).

The strongest correlation of the estimated potential was to the observed magnetic field magnitude $|B_{(IMF)}|$ (Figure 7a). We used Deming regression to fit for a line of best fit (red line). Higher values of the $|B_{(IMF)}|$ would increase the field strength in the magnetosheath and therefore would produce a lower plasma β (thermal to

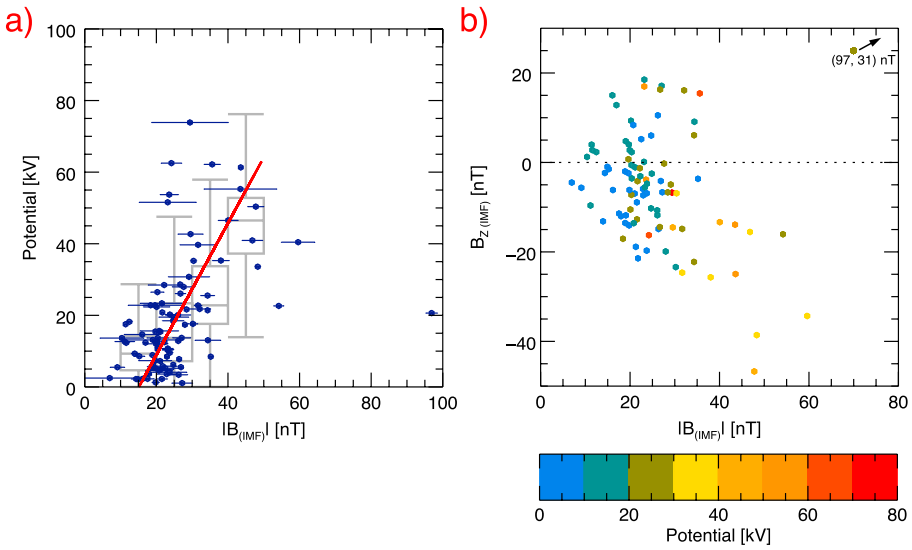

Figure 7. The plasma mantle potential estimates compared to the associated solar wind conditions: (a) the estimated cross-magnetospheric electric potential compared to the magnetic field magnitude of the IMF observed in the solar wind. The data are shown as box and whisker plots in gray, where the box represents the interquartile range (IQR); the central line shows that the median and the whisker length are 1.5 of the IQR. These box plots were calculated for solar wind conditions in groups of 10 nT (0–9.9, 10–19.9 nT, etc.). (b) The estimated potential dependence on both the IMF magnitude and the IMF B_Z.

magnetic pressure ratio) in the magnetosheath. A lower plasma β has been shown to make reconnection much more likely at the magnetopause (Swisdak et al., 2003) and has been observed at Mercury (DiBraccio et al., 2013).

A weak correlation was observed with both the B_{IMF} and the $B_{Z(IMF)}$ orientation (Figure 7b), with the potential on a colored scale. We see that the low potential estimates (bluer colors) are clustered at lower B_{IMF} values and B_Z values closer to 0 nT. For larger B_{IMF} (>35 nT) and more negative B_Z (<10 nT) the potential is generally higher (red colors). We can see that the potential is therefore dependent on both higher IMF magnitudes and more southward-orientated IMF.

Figure 8a shows the dependence of the observed magnetic field strength in the mantle to the IMF field magnitude. As the latter increases, so does the former. As the reconnection rate increases due to a higher IMF magnitude, more magnetic flux is transported from the dayside into the nightside, which increases the observed magnitude in the plasma mantle.

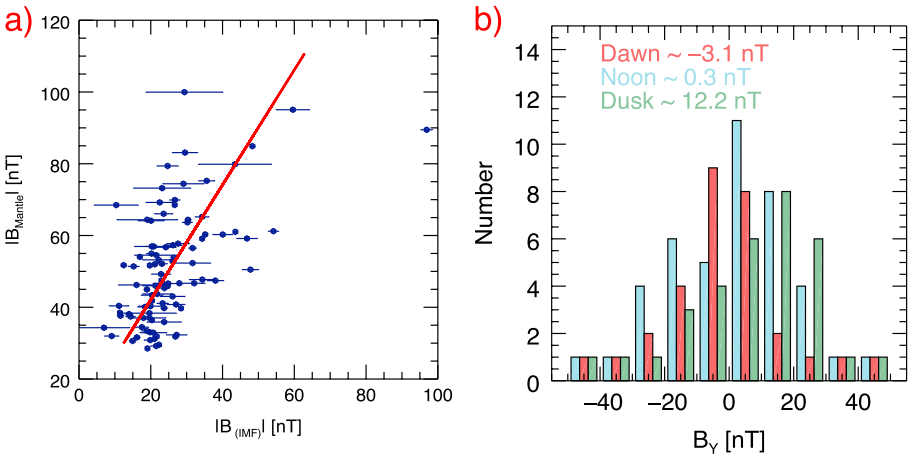

Figure 8. (a) The dependence of the observed mantle magnetic field strength on the IMF magnitude; (b) the location of the mantle observations compared to the B_Y orientation of the IMF. The mean IMF B_Y strength is shown at the top for each sector.

Figure 8b shows a histogram of the IMF B_Y component strength divided into three groups: blue for plasma mantle observations in the noon sector (23:00 to 01:00 local time in abberated coordinates), red for observations at dawn (after 01:00 LT), and green for observations at dusk (before 23:00 LT). The bins for noon observations peak near 0 nT, while the dawn and dusk bins peak for $-B_Y$ and $+B_Y$ IMF fields. Therefore, we can see a strong dependence of the location of the plasma mantle observation on the orientation of the IMF B_Y component. If the IMF has a large component in the $+B_Y$ direction, then the reconnected field line has a convection direction toward dusk, resulting in the plasma mantle to be more likely to be observed there. This effect has been previously observed at Earth (e.g., Cowley, Morelli, & Lockwood, 1991; Gosling et al., 1990; 2006).

3.7. Online Supporting Material

In the online supporting information we provide a list of mantle event times and we present the event described in the error discussion of section 3.3 (28 September 2011).

4. Discussion and Conclusions

4.1. Discussion

We have presented a survey of southern plasma mantle observations at Mercury's magnetosphere using data from the ion and magnetic field measurement taken by the FIPS and magnetometer instruments, respectively. There were 94 mantle crossings in the southern hemisphere analyzed in this study. The trajectory of the spacecraft is such that only the southern mantle is observed on consequent MESSENGER orbits. The plasma in the mantle forms as a consequence of magnetic reconnection on the dayside magnetopause that injects magnetosheath plasma into the magnetosphere, which then mirrors in the cusp and is traveling antisunward in the nightside tail. The average mantle proton and sodium number densities were found to be 1.5 and 0.004 cm^{-3}, respectively. Due to the northward offset of Mercury's magnetospheric dipole (Anderson et al., 2011), north-south asymmetries have been observed in the magnetospheric plasma measurements (Korth et al., 2014). We do not expect the southern plasma mantle characteristics presented here to represent the northern mantle due to the above-mentioned asymmetry.

We studied the IMF conditions for which these mantle observations took place in, by averaging the IMF outside the bow shock for 2 min (and 20 min to account for any variability). We also compared these observations to times when MESSENGER did not observe the mantle but could have (by location and field of view of the FIPS instrument). There were 957 orbits where one would expect to observe the plasma mantle in the MESSENGER data. This demonstrates that the plasma mantle is not a permanent feature of Mercury's magnetosphere. If we assume that reconnection at Mercury's dayside magnetopause is occurring near continuously, then this means that most of the particles injected into the cusp are lost to the planet (and do not mirror to form the plasma mantle). Superposed cusp ion observation analysis shows that ions are mainly observed to be flowing toward the planet with pitch angles of 0–90° measured in the northern cusp (Poh et al., 2016). These observations took place close to the mirror point, so we assume that most of these particles did not mirror and would not be able to form the mantle, supporting our idea that the mantle is not a permanent feature of Mercury's magnetosphere. However, there are limitations to this conclusion. The supporting work only superposed 16 cusp events (Poh et al., 2016). Although this gives a good presentation of the cusp, the number of events used is not large enough to give a more statistical idea of Mercury's cusp ions. Also, not observing the plasma mantle with MESSENGER does not mean that the mantle is not always there but could mean that the spacecraft did not cross at the correct local time, since the B_Y component of the IMF has a moderate effect on the mantles location. However, even with these limitations, the fact that the mantle is observed so little of the time ($<$10%), we would not expect MESSENGER to "miss" the mantle 90% of the time. Therefore, we believe that our conclusion is correct and the mantle is not a permanent feature of the nightside magnetosphere.

Comparing orbits when MESSENGER did not observe the mantle, we see that the mantle is more likely to be seen at IMF magnitudes less than ~30 nT. We attribute this to higher IMF magnitudes producing more intense reconnection at the dayside magnetopause. This is due to the higher parallel electric fields, which will more likely inject particles with field-aligned pitch angles, which will not mirror and therefore not produce an observable mantle (Egedal et al., 2012; Li et al., 2017).

The plasma mantle is observed for a variety of IMF orientations, which supports previous work (DiBraccio et al., 2013; Slavin et al., 2014) that reconnection at Mercury can occur for low shear angles. However, our results also show that reconnection still favors southward IMF orientations, with more plasma mantle events observed for $-B_Z$ IMF. This shows that Mercury does have an Earth-like response with a dependence on the B_Z orientation. We also find that $-B_X$ IMF conditions favor the southern mantle and therefore southern cusp. This agrees with previous results using remote sodium exospheric emission observations (Mangano et al., 2015; Massetti et al., 2017) but disagrees with previous modeling investigating this correlation (Massetti et al., 2007; Sarantos et al., 2001). We suggest that previous modeling results do not agree with the growing body of observational results because they do not explicitly focus their investigation into exploring this effect and therefore lack consistency between model runs. This B_X effect should, however, be investigated further.

The plasma mantle observations exhibit an ion energy dispersion. This is evident due to the trajectory of the spacecraft that is near orthogonal to the magnetopause. The tailward traveling ions experience an $\mathbf{E} \times \mathbf{B}$ drift toward the plasma sheet. Ions with higher energies have a larger parallel velocity, and therefore, their tailward motion is less affected by the $\mathbf{E} \times \mathbf{B}$ drift in comparison to lower-energy ions. This means that higher energy ions are observed nearer the magnetopause. Using this observed phenomenon, we calculate the ions $\mathbf{E} \times \mathbf{B}$ velocity to estimate the electric field and subsequently the cross-electric magnetospheric potential, Φ.

Φ is an important value to estimate as it is a measurement used to characterize the input of solar wind energy into a planet's magnetosphere. It is therefore useful in understanding a planet's coupling to the Sun. For Mercury, this value has been estimated in previous work, using different methods. Slavin et al. (2009) reported a value of ~30 kV during the second Mercury flyby by MESSENGER. Imber et al. (2014) used the flux content found in flux transfer events observed at Mercury to estimate a potential of ~25 kV, and DiBraccio et al. (2013) found an average of ~29 kV from dayside magnetopause crossings. Analyzing two plasma mantle case studies, DiBraccio, Slavin, Raines, et al. (2015) estimated values of ~23 and ~29 kV.

We find a wide spread of calculated potentials (1–74 kV), ~66% of the observations are below 20 kV, and ~80% are below 30 kV (see Figure 5d). The average is found to be ~19 kV and the median ~ 13 kV. Therefore, our results show that the potential is lower at Mercury than previously thought. However, this is not completely surprising considering that previous estimates focus on observations of large events, such as the FTEs observed by Imber et al. (2014) and one of the clearest plasma mantle crossings analyzed by DiBraccio, Slavin, Raines, et al. (2015). These studies are more likely to omit events when Mercury's magnetosphere is less dynamic and produces quieter, less intense observations. Our study focuses on a larger number events, is the first of its kind, and therefore is a more accurate representation of Mercury's magnetosphere. The wide spread of estimated cross-magnetospheric potentials reveals how dynamic Mercury's magnetosphere is and how much the solar wind interaction can vary.

The strongest correlation we found between the estimated potential and the IMF was the observed magnetic field magnitude of the interplanetary magnetic field (see Figure 7a). Stronger IMF magnitudes led to higher cross-magnetospheric potentials. However, we did not find as strong a correlation between the north-south (B_Z) component of the IMF and the potential as with the magnitude. We do, however, observe higher potentials when both the magnitude and $-B_Z$ are large (Figure 7b). These results support previous observations (DiBraccio et al., 2013) that reconnection at Mercury can occur for a variety of shear angles, unlike at Earth or the outer planets. However, 75% of our observations do occur with shear angles greater than 90°. This shows that although reconnection can occur at various shear angles at Mercury, Mercury is still very similar to other planets where reconnection is most likely to occur with higher rates when the IMF and magnetospheric field have a high shear angle like at Earth and the outer planets.

The calculated potentials are lower than the upper limit at Earth, ~200 kV (Kivelson & Ridley, 2008), and the reconnection voltages at the outer planets, Uranus and Neptune, which have been estimated to be ~40 and ~35 kV (Masters, 2014, 2015). These, however, are upper values that might not be observed due to ionospheric saturation effects. The cross-electric magnetospheric potential is affected by the ionospheric conductivity, which when high enough, affects the currents closing in the polar cap that then limit reconnection by affecting the magnetic field at the magnetopause (e.g., Hill, Dessler, & Wolf, 1976; Rassbach, Wolf, & Daniell, 1974), so that $\Phi \leq 2/3\ \Phi_{SW}$ (Slavin, 2004), for planets with a significant atmosphere. However, for

Mercury, this is closer to $\Phi \sim \Phi_{SW}$ due to the low conductivity of its ionosphere. Therefore, large values at Earth (150–200 kV) are rarely seen, with values closer to 50–100 kV considered more typical (e.g., Siscoe et al., 2002; Siscoe, Crooker, & Siebert, 2002). Consequently, the potentials calculated in this study are comparable or larger than those at Uranus and Neptune and usually lower than the values for Earth. The average of ~19 kV is also remarkably close to ~17 kV predicted by Hill et al. (1976).

Even after the end of this mission, the MESSENGER spacecraft is still providing insight into Mercury's highly dynamic and small magnetosphere. We have found that although Mercury's magnetosphere is the most highly driven by its interaction with the solar wind in comparison to other planets in the solar system, at times, it is not as highly driven by the solar wind as previously thought. This is mainly due to our study being statistical in nature, while previous reports have focused on large events. However, further work is required to elucidate the nature of this interaction, specifically the exact role of flux transfer events in a full comprehensive statistical survey.

4.2. Conclusions

We have presented and analyzed 94 observations of the southern plasma mantle, and 957 events when MESSENGER did not observe a plasma mantle in the south (and could have done with FIPS). From the plasma mantle observations we estimated the cross-electric magnetospheric potential. We have learnt the following:

1. For the southern plasma mantle the mean and median proton number density are 1.5 and 1.3 cm^{-3}, respectively, and for sodium number density, these values are 0.004 and 0.002 cm^{-3}.
2. The highest estimate of proton and sodium flux contribution of the mantle to the plasma sheet are 1.5×108 cm^{-2} s^{-1} and 0.8×108 cm^{-2} s^{-1}, respectively.
3. The formation of the plasma mantle is strongly dependent on the upstream IMF magnitude. The potential increases for larger IMF magnitudes; however, much higher magnitudes than ~30 kV are less likely to form a plasma mantle as the particles are less likely to mirror on the dayside.
4. Even though reconnection and particle injection can occur for all shear angles at Mercury, there is still a strong Earthlike preference for reconnection to occur for southward IMF orientations.
5. The southern mantle and therefore the southern cusp are more likely to be observed with antisunward ($-BX$) orientations.
6. The orientation of the IMF in the BY dictates whether the mantle is observed more duskward (for $+BY$) or more dawnward (for $-BY$) of the noon-midnight meridian.
7. The cross-electric potential is often lower than previous studies reported, which shows that at times, Mercury's magnetosphere can be less dynamic than previously thought.

Acknowledgments
This research was supported by the following grants: NASA's Discovery Data Analysis (NNX15AK88G), STROFIO Investigation Science Support from Southwest Research Institute (E99061MO), Living With a Star (NNX16AJ67G), NASA grant 14-DDAP14_2-0006, and NASA DDAP grant NNX16AJ05G. All the data used in this study can be found at NASA's Planetary Data System (https://pds.jpl.nasa.gov).

References

Anderson, B. J., Acuña, M. H., Lohr, D. A., Scheifele, J., Raval, A., Korth, H., & Slavin, J. A. (2007). The magnetometer instrument on MESSENGER. *Space Science Reviews*, *131*, 417. https://doi.org/10.1007/s11214-007-9246-7

Anderson, B. J., Johnson, C. L., Korth, H., Purucker, M. E., Winslow, R. M., Slavin, J. A., … Zurbuchen, T. H. (2011). The global magnetic field of Mercury from MESSENGER orbital observations. *Science*, *333*, 1859–1862. https://doi.org/10.1126/science.1211001

Andrews, G., Zurbuchen, T. H., Mauk, B. H., Malcom, H., Fisk, L. A., Gloeckler, G., … Raines, J. M. (2007). The energetic particle and plasma spectrometer instrument on the MESSENGER spacecraft. *Space Science Reviews*, *131*, 523. https://doi.org/10.1007/s11214-007-9272-5

Boardsen, S. A., Sundberg, T., Slavin, J. A., Anderson, B. J., Korth, H., Solomon, S. C., & Blomberg, L. G. (2010). Observations of Kelvin-Helmholtz waves along the dusk-side boundary of Mercury's magnetosphere during MESSENGER's third flyby. *Geophysical Research Letters*, *37*, L12101. https://doi.org/10.1029/2010GL043606

Burton, R. K., McPherron, R. L., & Russell, C. T. (1975). The terrestrial magnetosphere—A half-wave rectifier of the interplanetary electric field. *Science*, *189*, 717. https://doi.org/10.1126/science.189.4204.717

Cowley, S. W. H., Morelli, J. P., & Lockwood, M. (1991). Dependence of convective flows and particle precipitation in the high-latitude dayside ionosphere on the X and Y components of the interplanetary magnetic field. *Journal of Geophysical Research*, *96*, 5557–5564. https://doi.org/10.1029/90JA02063

Delcourt, D. C., Grimald, S., Leblanc, F., Berthelier, J.-J., Millilo, A., Mura, A., … Moore, T. E. (2003). A quantitative model of the planetary Na^+ contribution to Mercury's magnetosphere. *Annales de Geophysique*, *21*, 1723–1736. https://doi.org/doi:10.5194/angeo-21-1723-2003

DiBraccio, G. A., Slavin, J. A., Boardsen, S. A., Anderson, B. J., Korth, H., Zurbuchen, T. H., … Solomon, S. C. (2013). MESSENGER observations of magnetopause structure and dynamics at Mercury. *Journal of Geophysical Research: Space Physics*, *118*, 997–1008. https://doi.org/10.1002/jgra.50123

DiBraccio, G. A., Slavin, J. A., Imber, S. M., Gershman, D. J., Raines, J. M., Jackman, C. M., … Solomon, S. C. (2015). MESSENGER observations of flux ropes in Mercury's magnetotail. *Planetary and Space Science*, *115*, 77–89. https://doi.org/10.1016/j.pss.2014.12.016

DiBraccio, G. A., Slavin, J. A., Raines, J. M., Gershman, D. J., Tracy, P. J., Boardsen, S. A., … Solomon, S. C. (2015). First observations of Mercury's plasma mantle by MESSENGER. *Geophysical Research Letters*, *42*, 9666–9675. https://doi.org/10.1002/2015GL065805

Dungey, J. W. (1961). Interplanetary magnetic field and the auroral zones. *Physical Review Letters*, *6*, 47–48. https://doi.org/10.1103/PhysRevLett.6.47

Egedal, J., Daughton, W., & Le, A. (2012). Large-scale electron acceleration by parallel electric fields during magnetic reconnection. *Nature Physics*, *8*, 321–324. https://doi.org/10.1038/nphys2249

Fu, Z. F., & Lee, L. C. (1985). Simulation of multiple X-line reconnection at the dayside magnetopause. *Geophysical Research Letters*, *12*, 291–294. https://doi.org/10.1029/GL012i005p00291

Gershman, D. J., Slavin, J. A., Raines, J. M., Zurbuchen, T. H., Anderson, B. J., Korth, H., … Solomon, S. C. (2013). Magnetic flux pileup and plasma depletion in Mercury's subsolar magnetosheath, *Journal of Geophysical Research: Space Physics*, *118*, 7181–7199. https://doi.org/10.1002/2013JA019244

Gershman, D. J., Zurbuchen, T. H., Fisk, L. A., Gilbert, J. A., Raines, J. M., Anderson, B. J., … Solomon, S. C. (2012). Solar wind alpha particles and heavy ions in the inner heliosphere observed with MESSENGER. *Journal of Geophysical Research*, *117*, A00M02. https://doi.org/10.1029/2012JA017829

Gosling, J. T., Thomsen, M. F., Bame, S. J., Elphic, R. C., & Russell, C. T. (1990). Plasma flow reversals at the dayside magnetopause and the origin of asymmetric polar cap convection. *Journal of Geophysical Research*, *95*, 8073–8084. https://doi.org/10.1029/JA095iA06p08073

Hill, T. W., Dessler, A. J., & Wolf, R. A. (1976). Mercury and Mars: The role of ionospheric conductivity in the acceleration of magnetospheric particles. *Geophysical Research Letters*, *3*, 429–432. https://doi.org/10.1029/GL003i008p00429

Ho, G., Raines, J. M., Nguyen, L., Gannon, M., & Reid, M. (2016). MESSENGER: Software interface specification for the derived records of the energetic particle and plasma spectrometer, NASA Planetary Data System, MESS-E_V_H_SW-EPPS-3-FIPS-DDR-V2.0.

Hones, E. W. Jr., Asbridge, J. R., Bame, S. J., Montgomery, M. D., Singer, S., & Akasofu, S.-I. (1972). Measurements of magnetotail plasma flow made with Vela 4B. *Journal of Geophysical Research*, *77*, 5503–5522. https://doi.org/10.1029/JA077i028p05503

Horowitz, J. L., & Moore, T. E. (1997). Four contemporary issues concerning ionospheric plasma flow to the magnetosphere. *Space Science Reviews*, *80*, 49–76.

Huang, C.-S. (2002). Evidence of periodic (2–3 hour) near-tail magnetic reconnection and plasmoid formation: Geotail observations. *Geophysical Research Letters*, *29*(24), 2189. https://doi.org/10.1029/2002GL016162

Imber, S. M., Slavin, J. A., Boardsen, S. A., Anderson, B. J., Korth, H., McNutt, R. L. Jr., … Solomon, S. C. (2014). MESSENGER observations of large dayside flux transfer events: Do they drive Mercury's substorm cycle? *Journal of Geophysical Research: Space Physics*, *119*, 5613–5623. https://doi.org/10.1002/2014JA019884

Jasinski, J. M., Arridge, C. S., Lamy, L., Leisner, J. S., Thomsen, M. F., Mitchell, D. G., … Waite, J. H. (2014). Cusp observation at Saturn's high-latitude magnetosphere by the Cassini spacecraft. *Geophysical Research Letters*, *41*, 1382–1388. https://doi.org/10.1002/2014GL059319

Jasinski, J. M., Slavin, J. A., Arridge, C. S., Poh, G., Jia, X., Sergis, N., … Waite, J. H. Jr. (2016). Flux transfer event observation at Saturn's dayside magnetopause by the Cassini spacecraft. *Geophysical Research Letters*, *43*, 6713–6723. https://doi.org/10.1002/2016GL069260

Jia, X., Slavin, J. A., Gombosi, T. I., Daldorff, L. K. S., Toth, G., & van der Holst, B. (2015). Global MHD simulations of Mercury's magnetosphere with coupled planetary interior: Induction effect of the planetary conducting core on the global interaction. *Journal of Geophysical Research: Space Physics*, *120*, 4763–4775. https://doi.org/10.1002/2015JA021143

Johnson, C. L., Purucker, M. E., Korth, H., Anderson, B. J., Winslow, R. M., Al Asad, M. M. H., … Solomon, S. C. (2012). MESSENGER observations of Mercury's magnetic field structure. *Journal of Geophysical Research*, *117*, E00L14. https://doi.org/10.1029/2012JE004217

Kivelson, M. G., & Ridley, A. J. (2008). Saturation of the polar cap potential: Inference from Alfve'n wing arguments. *Journal of Geophysical Research*, *113*, A05214. https://doi.org/10.1029/2007JA012302

Korth, H., Anderson, B. J., Gershman, D. J., Raines, J. M., Slavin, J. A., Zurbuchen, T. H., … McNutt, R. L. Jr. (2014). Plasma distribution in Mercury's magnetosphere derived from MESSENGER magnetometer and fast imaging plasma spectrometer observations. *Journal of Geophysical Research: Space Physics*, *119*, 2917–2932. https://doi.org/10.1002/2013JA019567

Li, X., Guo, F., Li, H., & Li, G. (2017). Particle acceleration during magnetic reconnection in a low-beta plasma. *The Astrophysical Journal*, *843*, 1. https://doi.org/10.3847/1538-4357/aa745e

Lockwood, M., & Smith, M. F. (1994). Low and middle altitude cusp particle signatures for general magnetopause reconnection rate variations: 1. Theory. *Journal of Geophysical Research*, *99*, 8531–8553. https://doi.org/10.1029/93JA03399

Mangano, V., Massetti, S., Milillo, A., Plainaki, C., Orsini, S., Rispoli, R., & Leblanc, F. (2015). THEMIS Na exosphere observations of Mercury and their correlation with in-situ magnetic field measurements by MESSENGER. *Planetary and Space Science*, *115*, 102–109. https://doi.org/10.1016/j.pss.2015.04.001

Massetti, S., Mangano, V., Milillo, A., Mura, A., Orsini, S., & Plainaki, C. (2017). Short-term observations of double-peaked Na emission from Mercury's exosphere. *Geophysical Research Letters*, *44*, 2970–2977. https://doi.org/10.1002/2017GL073090

Massetti, S., Orsini, S., Milillo, A., & Mura, A. (2007). Modelling Mercury's magnetosphere and plasma entry through the dayside magnetosphere. *Planetary and Space Science*, *55*, 1557–1568. https://doi.org/10.1016/j.pss.2006.12.008

Masters, A. (2014). Magnetic reconnection at Uranus' magnetopause. *Journal of Geophysical Research: Space Physics*, *119*, 5520–5538. https://doi.org/10.1002/2014JA020077

Masters, A. (2015). Magnetic reconnection at Neptune's magnetopause. *Journal of Geophysical Research: Space Physics*, *120*, 479–493. https://doi.org/10.1002/2014JA020744

Milan, S. E., Provan, G., & Hubert, B. (2007). Magnetic flux transport in the Dungey cycle: A survey of dayside and nightside reconnection rates. *Journal of Geophysical Research*, *112*, A01209. https://doi.org/10.1029/2006JA011642

Mozer, F. S., & Retin'o, A. (2007). Quantitative estimates of magnetic field reconnection properties from electric and magnetic field measurements. *Journal of Geophysical Research*, *112*, A10206. https://doi.org/10.1029/2007JA012406

Pilipp, W. G., & Morfill, G. (1978). The formation of the plasma sheet resulting from plasma mantle dynamics. *Journal of Geophysical Research*, *83*, 5670–5678. https://doi.org/10.1029/JA083iA12p05670

Pitout, F., Escoubet, C. P., Klecker, B., & Rème, H. (2006). Cluster survey of the mid-altitude cusp: 1. size, location, and dynamics. *Annales de Geophysique*, *24*, 3011–3026. https://doi.org/10.5194/angeo-24-3011-2006

Poh, G., Slavin, J. A., Jia, X., DiBraccio, G. A., Raines, J. M., … Solomon, S. C. (2016). MESSENGER observations of cusp plasma filaments at Mercury. *Journal of Geophysical Research: Space Physics*, *121*, 8260–8285. https://doi.org/10.1002/2016JA022552

Poh, G., Slavin, J. A., Jia, X., Raines, J. M., Imber, S. M., Sun, W.-J., … Smith, A. W. (2017). Mercury's cross-tail current sheet: Structure, X-line location and stress balance. *Geophysical Research Letters*, *44*, 678–686. https://doi.org/10.1002/2016GL071612

Raines, J. M., Gershman, D. J., Slavin, J. A., Zurbuchen, T. H., Korth, H., Anderson, B. J., & Solomon, S. C. (2014). Structure and dynamics of Mercury's magnetospheric cusp: MESSENGER measurements of protons and planetary ions. *Journal of Geophysical Research: Space Physics*, *119*, 6587–6602. https://doi.org/10.1002/2014JA020120

Raines, J. M., Slavin, J. A., Zurbuchen, T. H., Gloeckler, G., Anderson, B. J., Baker, D. N., … McNutt, R. L. Jr. (2011). MESSENGER observations of the plasma environment near Mercury. *Planetary and Space Science*, *59*, 2004–2015. https://doi.org/10.1016/j.pss.2011.02.004

Rassbach, M. E., Wolf, R. A., & Daniell, R. E. Jr. (1974). Convection in a Martian magnetosphere. *Journal of Geophysical Research*, *79*, 1125–1127. https://doi.org/10.1029/JA079i007p01125

Reiff, P. H., Hill, T. W., & Burch, J. L. (1977). Solar wind plasma injection at the dayside magnetospheric cusp. *Journal of Geophysical Research*, *82*, 479–491. https://doi.org/10.1029/JA082i004p00479

Rijnbeek, R. P., Cowley, S. W. H., Southwood, D. J., & Russell, C. T. (1984). A survey of dayside flux transfer events observed by ISEE 1 and 2 magnetometers. *Journal of Geophysical Research*, *89*, 786–800. https://doi.org/10.1029/JA089iA02p00786

Rosenbauer, H., Grünwaldt, H., Montgomery, M. D., Paschmann, G., & Sckopke, N. (1975). Heos 2 plasma observations in the distant polar magnetosphere: The plasma mantle. *Journal of Geophysical Research*, *80*, 2723–2737. https://doi.org/10.1029/JA080i019p02723

Russell, C. T., & Elphic, R. C. (1978). Initial ISEE magnetometer results—Magnetopause observations. *Space Science Reviews*, *22*, 681–715. https://doi.org/10.1007/BF00212619

Russell, C. T., & Elphic, R. C. (1979). ISEE observations of flux transfer events at the dayside magnetopause. *Geophysical Research Letters*, *6*, 33–36. https://doi.org/10.1029/GL006i001p00033

Sanchez, E. R., & Siscoe, G. L. (1990). IMP 8 magnetotail boundary crossings: A test of the MHD models for an open magnetosphere. *Journal of Geophysical Research*, *95*, 20,771–20,779. https://doi.org/10.1029/JA095iA12p20771

Sarantos, M., Reiff, P. H., Hill, T. W., Killen, R. M., & Urquhart, A. L. (2001). A Bx-interconnected magnetosphere model for Mercury. *Planetary and Space Science*, *49*(14–15), 1629–1635. https://doi.org/10.1016/S0032-0633(01)00100-3

Sckopke N., Grunwaldt, H., Montgomery, M. D., Paschmannan, G., & Rosenbauer, H. (1973). Observations of proton flow inside the high latitude magnetopause with the MPI plasma experiment on Heos 2. Paper presented at Chapman Memorial Symposium on Magnetospheric Motions, AGU, Boulder, CO. 18–22 June.

Sckopke, N., & Paschmann, G. (1978). The plasma mantle. A survey of magnetotail boundary layer observations. *Journal of Atmospheric and Terrestrial Physics*, *40*(3), 261–278. https://doi.org/10.1016/0021-9169(78)90044-2

Sckopke, N., Paschmann, G., Rosenbauer, H., & Fairfield, D. H. (1976). Influence of the interplanetary magnetic field on the occurrence and thickness of the plasma mantle. *Journal of Geophysical Research*, *81*, 2687–2691. https://doi.org/10.1029/JA081i016p02687

Shue, J.-H., Chao, J. K., Fu, H. C., Russell, C. T., Song, P., Khurana, K. K., & Singer, H. J. (1997). A new functional form to study the solar wind control of the magnetopause size and shape. *Journal of Geophysical Research*, *102*, 9497–9511. https://doi.org/10.1029/97JA00196

Siscoe, G. L., Crooker, N. U., & Siebert, K. D. (2002). Transpolar potential saturation: Roles of region 1 current system and solar wind ram pressure. *Journal of Geophysical Research*, *107*(A10), 1321. https://doi.org/10.1029/2001JA009176

Siscoe, G. L., Erickson, G. M., Sonnerup, B. U. Ö., Maynard, N. C., Schoendorf, J. A., Siebert, K. D., … Wilson, G. R. (2002). Hill model of transpolar potential saturation: Comparisons with MHD simulations. *Journal of Geophysical Research*, *107*(A6), 1075. https://doi.org/10.1029/2001JA000109

Siscoe, G. L., Ness, N. F., & Yeates, C. M. (1975). Substorms on Mercury? *Journal of Geophysical Research*, *80*, 4359–4363. https://doi.org/10.1029/JA080i031p04359

Siscoe, G. L., & Sanchez, E. (1987). An MHD model for the complete open magnetotail boundary. *Journal of Geophysical Research*, *92*, 7405–7412. https://doi.org/10.1029/JA092iA07p07405

Slavin, J. A. (2004). Mercury's magnetosphere. *Advances in Space Research*, *33*(11), 1859–1874. https://doi.org/10.1016/j.asr.2003.02.019

Slavin, J. A., Acuña, M. H., Anderson, B. J., Baker, D. N., Benna, M., Boardsen, S. A., … Zurbuchen, T. H. (2009). MESSENGER observations of magnetic reconnection in Mercury's magnet osphere. *Science*, *324*, 606–610. https://doi.org/10.1126/Science.1172011

Slavin, J. A., Anderson, B. J., Baker, D. N., Benna, M., Boardsen, S. A., Gloeckler, G., … Zurbuchen, T. H. (2010). MESSENGER observations of extreme loading and unloading of Mercury's magnetic tail. *Science*, *329*, 665–668. https://doi.org/10.1126/Science.1188067

Slavin, J. A., DiBraccio, G. A., Gershman, D. J., Imber, S. M., Poh, G. K., Raines, J. M., … Solomon, S. C. (2014). MESSENGER observations of Mercury's dayside magnetosphere under extreme solar wind conditions. *Journal of Geophysical Research: Space Physics*, *119*. 8087–8116. https://doi.org/10.1002/2014JA020319

Slavin, J. A., Imber, S. M., Boardsen, S. A., DiBraccio, G. A., Sundberg, T., Sarantos, M., … Solomon, S. C. (2012). MESSENGER observations of a flux-transfer-event shower at Mercury. *Journal of Geophysical Research*, *117*, A00M06. https://doi.org/10.1029/2012JA017926

Slavin, J. A., Smith, E. J., Sibeck, D. G., Baker, D. N., Zwickl, R. D., & Akasofu, S.-I. (1985). An ISEE 3 study of average and substorm conditions in the distant magnetotail. *Journal of Geophysical Research*, *90*, 10,875–10,895. https://doi.org/10.1029/JA090iA11p10875

Sun, W. J., Fu, S. Y., Slavin, J. A., Raines, J. M., Zong, Q. G., Poh, G. K., & Zurbuchen, T. H. (2016). Spatial distribution of Mercury's flux ropes and reconnection fronts: MESSENGER observations. *Journal of Geophysical Research: Space Physics*, *121*, 7590–7607. https://doi.org/10.1002/2016JA022787

Sun, W.-J., Slavin, J. A., Fu, S., Raines, J. M., Zong, Q.-G., Imber, S. M., & Baker, D. N. (2015). MESSENGER observations of magnetospheric substorm activity in Mercury's near magnetotail. *Geophysical Research Letters*, *42*, 3692–3699. https://doi.org/10.1002/2015GL064052

Sundberg, T., Slavin, J. A., Boardsen, S. A., Anderson, B. J., Korth, H., Ho, G. C., … Solomon, S. C. (2012). MESSENGER observations of dipolarization events in Mercury's magnetotail. *Journal of Geophysical Research*, *117*, A00M03. https://doi.org/10.1029/2012JA017756

Swisdak, M., Rogers, B. N., Drake, J. F., & Shay, M. A. (2003). Diamagnetic suppression of component magnetic reconnection at the magnetopause. *Journal of Geophysical Research*, *108*(A5), 1218. https://doi.org/10.1029/2002JA009726

Tanskanen, E. I. (2009). A comprehensive high-throughput analysis of substorms observed by IMAGE magnetometer network: Years 1993–2003 examined. *Journal of Geophysical Research*, *114*, A05204. https://doi.org/10.1029/2008JA013682

Winslow, R. M., Anderson, B. J., Johnson, C. L., Slavin, J. A., Korth, H., Purucker, M. E., … Solomon, S. C. (2013). Mercury's magnetopause and bow shock from MESSENGER Magnetometer observations. *Journal of Geophysical Research: Space Physics*, *118*, 2213–2227. https://doi.org/10.1002/jgra.50237